UAV Splay State Configuration for Moving Targets in Wind

Derek Kingston and Randal Beard

Brigham Young University

Abstract. Cooperative surveillance problems require members of a team to spread out in some fashion to maximize coverage. In the case of single target surveillance, a team of UAVs angularly spaced (i.e. in the splay state configuration) provides the best coverage of the target in a wide variety of circumstances. In this chapter we propose a decentralized algorithm to achieve the splay state configuration for a team of UAVs tracking a moving target. We derive the allowable bounds on target velocity to generate a feasible solution as well as show that, near equilibrium, the overall system is exponentially stable. Monte Carlo simulations indicate that the surveillance algorithm is asymptotically stable for arbitrary initial conditions. We conclude with high fidelity simulation tests to show the applicability of the splay state controller to actual unmanned air systems.

1 Introduction

A primary use of unmanned air vehicle (UAV) systems is in surveillance and reconnaissance missions [1] [2]. We investigate the use of a team of multiple UAVs orbiting a target with application to target tracking and convoy support.

The payload of choice for most small UAVs is a camera. The objective of our work is to develop a cooperative guidance strategy to distribute UAV agents around an orbit spaced equally in angle. The equal angle spacing allows the team to cooperatively overcome possible line-of-sight occlusions, i.e. equal spacing gives the team the best chance to track a target in the presence of occlusions. We note that for two UAVs carrying radar sensors, line-of-sight angles separated by 90 degrees provide better statistical performance in the tracking problem [3] and when the team size is greater than two, equal spacing has good performance. In a general surveillance mission, the equal spacing of the sensors provides the best overall coverage of a target and its surroundings.

The design of a spacing controller is strongly influenced by the capabilities of the UAVs on the team. For instance, helicopters can hover at a specific location and thereby maintain persistant coverage of a ground based target, however fixed-wing aircraft must fly above the stall velocity, and may therefore not be able to maintain persistent coverage. Furthermore, fixed-wing aircraft fly most efficiently at a fixed, nominal airspeed. One approach to equal spacing is to adjust the local velocity of the agents along the desired orbit. However, for small allowable velocity bounds, the convergence to the equilibrium configuration may

M.J. Hirsch et al. (Eds.): Adv. in Cooper. Ctrl. & Optimization, LNCIS 369, pp. 109–128, 2007.
springerlink.com

be sluggish. Additionally, maintaining fixed-wing aircraft at their constant fuel efficient velocity is desirable from a mission duration standpoint. In this chapter we develop a spacing controller that steers the UAVs to the desired configuration while holding a constant airspeed.

Other researchers have studied the problem of spacing fixed-speed UAVs around a possibly moving target. Paley et al. introduce the notion of the splay state configuration and give an elegant control solution for fixed target problems [4]. Their approach relies on invariant set arguments to show that the splay state configuration is the stable equilibrium of the system. The main drawback of their work is the inability to specify the orbit center. The splay state configuration is shown to be stable around the collective center of mass *not* a specific target location which makes tracking a moving target infeasible without modifications. Additionally, the control signal exhibits slow transient response for large initial errors.

Paley's splay state configuration work is extended by Klein and Morgansen in [5] to moving targets. By choosing a control signal that preserves the invariant sets introduced by Paley, they are able to design an algorithm to track a moving target in the splay state configuration with 3 UAVs. Unfortunately, the method does not currently extend to team sizes other than $N = 3$.

Frew and Lawrence [1] use vector field notions to steer a team of two UAVs to an orbit centered on a moving target. A limit cycle is designed as the equilibrium of the vector field dynamics and is modified to account for spacing errors. No formal proof is offered in their method and only team sizes of $N = 2$ are considered.

The unique features of our approach are the ability to include an arbitrary number of team members in a moving target scenario and the determination of bounds on target velocity for which the algorithm satisfies the UAV's kinematic constraints. Additionally, the transient response is qualitatively better than other approaches. Of note is that our algorithm is completely decentralized where agents base their actions only on communication from immediate team members. This allows for dynamic changes to the team to be accounted for without global communication or replanning. A drawback to our approach is that global stability is not conclusively shown, although Monte-Carlo simulations indicate that the splay state configuration is the globally stable equilibrium of the system.

The aim of this chapter is to present a stable, decentralized spacing controller for fixed velocity UAVs tracking moving targets in the presence of wind. Section 2 formally defines the notion of equal spacing and describes the mathematical model that we use for the UAVs. Section 3 establishes the heading design for a group of UAVs monitoring a stationary target. In Section 4, we analyze the stability of the system for the stationary target case. These results are extended to the moving target/wind case in Section 5 and we conclude with simulation results in Section 6. Concluding remarks are offered in Section 7.

2 Problem Description

In a variety of applications the ability for a team of UAVs to spread out in some manner increases the efficiency of the team as a whole. For single target surveil-

lance, a team of UAVs spaced equally around an orbit centered on the target gives the best line-of-sight coverage in the presence of occlusions. This chapter focuses on constructing a desired heading for each UAV in the team to achieve equal spacing. The desired heading is calculated based on the distance away from the desired orbit and the spacing error from the splay state configuration.

Definition 1 (Splay State Configuration). *A set of agents $\mathcal{I}$, all of which are following the same periodic trajectory, is said to have reached the* splay state configuration *if for each agent i, the time difference of arrival to a specific point on the trajectory between agent i and its two immediate neighbors is constant for all $i \in \mathcal{I}$.*

Definition 1 describes the splay state configuration as equally spaced in time along a periodic trajectory. When agents pass a reference point (arbitrarily chosen) on the trajectory at equal time intervals, the team has reached the splay state configuration. For simple circular trajectories, the splay state configuration is achieved when agents are equally spaced in angle around the circle perimeter. Note that equal angular spacing matches the definition of the splay state configuration in [4]. Definition 1 extends the splay state notion to non-circular trajectories which occur when the center of the desired orbit is changing in time due to wind or target motion.

Consider a circular trajectory with all agents traveling at constant speed V. The time difference of arrival corresponds to the angle separation between neighbors. When the angle between all agents is the same then the splay state configuration has been reached, i.e. the agents are equally spaced in angle around the circle. Now consider the trajectory shown in Figure 1, which is an example of a UAV orbiting a moving target. Note that as the target speed increases, the ability for the UAV to maintain an orbit around the target depends on its ability to make increasingly sharp turns. Constraints on the turning radius of the UAV will lead to a threshold value of target speed where feasible tracking is no longer possible (see Section 5). In a moving reference frame (with the target in the

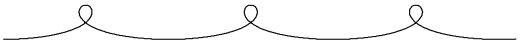

Fig. 1. For a UAV orbiting a moving target, the trajectory exhibits loops corresponding to the times when the UAV and the target are moving in opposite directions and long arcs when both are moving in the same direction

center) the motion of the UAV traces out a circle, but the splay state configuration does *not* correspond to equal spacing in angle around that circle. Since the target is moving, a much greater amount of time is spent on the part of the trajectory where the UAV and the target are moving in the same direction. When the target and UAV are moving in opposite directions, the UAV quickly travels around a large portion of the circle. Figure 2 shows the splay state configuration for 5 UAVs when the target is moving at 75% of V in zero wind conditions.

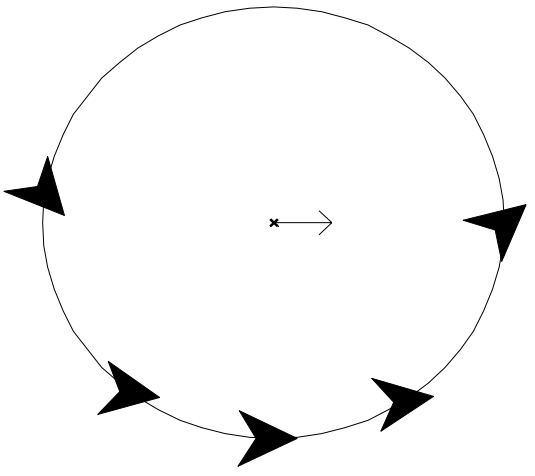

Fig. 2. A target moving at 75% of UAV speed has a splay state configuration with 5 vehicles that corresponds to the spacing in this figure. Note that at the bottom of the orbit, the target and the UAV are moving in the same direction, so the UAV slowly turns the corner. However, at the top of the orbit, the UAV and the target are moving in opposite directions, so the UAV quickly moves around the arc.

2.1 UAV Modeling

To maximize fuel efficiency each UAV maintains a constant airspeed. Additionally, we assume that all UAVs fly at a fixed altitude. A kinematic model for a constant airspeed, constant altitude UAV in wind, is given by

$$\begin{aligned} \dot{p}_N &= V_a \cos\psi + V_w \cos\psi_w \\ \dot{p}_E &= V_a \sin\psi + V_w \sin\psi_w \\ \dot{\psi} &= \tfrac{g}{V_a} \tan\phi \\ \dot{\phi} &= u \end{aligned} \tag{1}$$

where (p_N, p_E) are the (North, East) coordinates of the UAV in a flat earth model, ψ is the heading of the UAV (with the $\dot{\psi}$ equation given by the coordinated turn assumption), ϕ is the roll angle, V_a is the constant airspeed of the vehicle, V_w is the magnitude of the wind vector and ψ_w is the heading of the wind vector (note that this is not the meteorological definition of wind heading, i.e. ψ_w is the direction the wind is blowing *to* as opposed to the direction the wind is blowing *from*). In addition to these dynamics, a constraint on roll angle $-\phi_{\max} \leq \phi \leq \phi_{\max}$ is enforced that stall conditions are avoided.

We consider the motion of the UAV relative to a target position. Let

$$\begin{aligned} x &= p_N - q_N \\ y &= p_E - q_E \end{aligned} \tag{2}$$

where $(q_N,\ q_E)$ is the position of the target. The dynamics of (1) become

$$\begin{aligned} \dot{x} &= V_a \cos\psi + W_x \\ \dot{y} &= V_a \sin\psi + W_y \\ \dot{\psi} &= \tfrac{g}{V_a} \tan\phi \\ \dot{\phi} &= u \end{aligned} \tag{3}$$

where $W_x = V_w \cos\psi_w - \dot{q}_N$ and $W_y = V_w \sin\psi_w - \dot{q}_E$. Target velocity and wind are indistinguishable with respect to the relative motion of the UAV to the target. This allows the control design to maintain constant airspeed and account for wind disturbances and target motion with only regard to $(W_x,\ W_y)$.

Model (3) can be reduced further by letting

$$u = \frac{gV_a\dot{\omega}}{g^2 + V_a^2\omega^2}$$

where ω is the heading rate of the UAV, i.e. $\omega = \frac{g}{V_a}\tan\phi$. Model (3) then becomes the kinematic unicycle model

$$\begin{aligned} \dot{x} &= V_a \cos\psi + W_x \\ \dot{y} &= V_a \sin\psi + W_y \\ \dot{\psi} &= \omega \end{aligned} \tag{4}$$

where we constrain $|\omega| \leq \frac{g}{V_a}\tan(\phi_{\max})$ to ensure that $|\phi| \leq \phi_{\max}$. The constraint on ω can be thought of as a curvature constraint on the system kinematics from which it follows that the UAV can be considered a Dubins-type vehicle. This model has shown great value for design of UAV systems as it captures the essential navigational kinematics of UAV motion while at the same time being of low enough order to allow tractable analysis [2] [6] [7].

The heading design and analysis is performed at a level of abstraction greater than the unicycle level by computing a desired heading ψ^d and using it as a feed-forward term to the model (4). Feedback is then introduced at the control signal ω while maintaining the saturation constraints on ω. Let

$$\omega = \dot{\psi}^d + \nu \tag{5}$$

where ν is the feedback term driving ψ to ψ^d. This chapter shows that ψ^d can be chosen so that a team of UAVs with individual dynamics

$$\begin{aligned} \dot{x} &= V_a \cos\psi^d \\ \dot{y} &= V_a \sin\psi^d \end{aligned} \tag{6}$$

can reach the splay state configuration. Control gains in the calculation of ψ^d can then be chosen to allow the saturation constraints on ω to be satisfied. Note that ψ^d can be considered a sliding surface along which the specifications of the mission are satisfied. If ψ reaches ψ^d in finite time via the feedback term ν, then the overall system can be guaranteed to converge to the splay state configuration. Theoretically, a sliding mode controller of the form

$$\nu = \beta \text{sign}(\psi - \psi^d)$$

ensures that ψ reaches ψ^d in finite time, however in practice, a control law of the form

$$\nu = \beta \text{sat}\left(\frac{\psi - \psi^d}{\epsilon}\right)$$

is used, where β is a positive control gain. We do not show the overall system stability with this control strategy, but refer the reader to [8] where this choice of ν is shown to ensure path convergence for an arbitrary path in the single UAV case.

2.2 Orbit Dynamics

We will be concerned with the behavior of UAV teams while orbiting a target at a fixed radius R_{nom}. To analyze the stability of the orbit system, we make a change of variables by letting

$$\begin{aligned} R &= \sqrt{x^2 + y^2} \\ \theta &= \tan^{-1}\left(\tfrac{y}{x}\right) \end{aligned} \tag{7}$$

where R is the distance of the UAV from the target and θ is the "clock angle" of the UAV around the orbit.

In the static target, no wind case (i.e. $W_x = W_y = 0$), the dynamics of R and θ can be calculated as follows. Let

$$\chi \triangleq \psi - \psi^p \tag{8}$$

be the difference between the actual heading, ψ, and the heading of the tangent vector to the orbit, i.e. $\psi^p = \theta + \pi/2$. Therefore $\dot{R}$ can be calculated as

$$\begin{aligned} \dot{R} &= \tfrac{d}{dt}\sqrt{x^2 + y^2} \\ &= \tfrac{x\dot{x} + y\dot{y}}{\sqrt{x^2+y^2}} \\ &= \tfrac{V_a}{R}\left[x\cos\psi + y\sin\psi\right] \quad . \end{aligned}$$

Since $\psi = \chi + \theta + \pi/2$, we obtain

$$\dot{R} = \frac{V_a}{R}\left[-x\sin(\chi+\theta) + y\cos(\chi+\theta)\right] \quad .$$

Using the relations $\frac{x}{R} = \cos\theta$ and $\frac{y}{R} = \sin\theta$ we get that

$$\begin{aligned} \dot{R} &= -V_a\left[\cos\theta\sin(\chi+\theta) - \sin\theta\cos(\chi+\theta)\right] \\ &= -V_a\left\{\sin\chi\cos^2\theta + \cos\chi\sin\theta\cos\theta - \cos\chi\sin\theta\cos\theta + \sin\chi\sin^2\theta\right\} \\ \Rightarrow \dot{R} &= -V_a\sin\chi \quad . \end{aligned}$$

Similar arguments are used to derive the equation of motion for θ resulting in

$$\begin{aligned} \dot{R} &= -V_a\sin\chi \\ \dot{\theta} &= \frac{V_a}{R}\cos\chi \quad . \end{aligned} \tag{9}$$

In the case of a moving target and/or wind, the motion is abstracted by calculating the path heading ψ^p, i.e. the heading which the UAV should be traveling if directly on the path. By accounting for target motion and wind via the ψ^p term, the radial orbit dynamics remain identical to those in (9) [8]. We show in Section 5 the calculation of ψ^p for moving targets.

To accommodate the multiple UAV splay state configuration, a spacing term is defined. For the static target, no wind scenario, the separation of the i^{th} agent from the angular mean of its neighbors is

$$\delta\theta_i = \frac{1}{2}\left((\theta_i - \theta_{i-1}) - (\theta_{i+1} - \theta_i)\right) \tag{10}$$

where a ring topology is assumed (i.e. addition is defined modulo N). The term $\delta\theta_i$ captures how far away agent i is from being equally spaced between its two immediate neighbors on the ring. When all agents are on the nominal radius with spacing terms $\delta\theta_i$ equal to zero, then the team has achieved the splay state configuration. Although the calculation of $\delta\theta_i$ is more complicated in the moving target case, the principle is the same: $\delta\theta_i$ captures how far away from the splay state configuration agent i is with regards to its immediate neighbors along the ring.

A visual representation of the notation used to describe the desired heading calculation is shown in Figure 3 where d_i is the radial error from the nominal radius, i.e. $d_i \triangleq R_i - R_{\text{nom}}$.

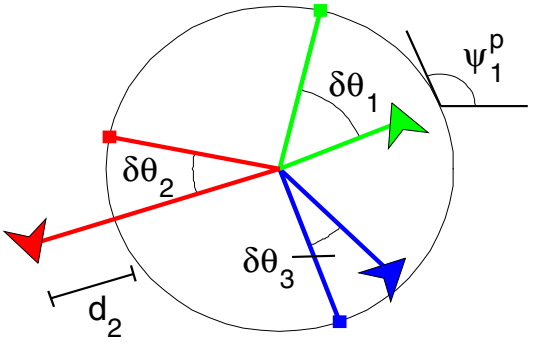

Fig. 3. Spacing error and radial error are combined to construct a desired heading for each UAV. Radial error is determined by the distance from the desired orbit (d_i) and spacing error is the distance from the angular center of an agent's two immediate neighbors ($\delta\theta_i$).

3 Heading Calculation for Non-moving Targets

This section details the construction of a desired heading to achieve the splay state configuration in the case of zero wind and a non-moving target. The basis of the splay state configuration controller is the calculation of an appropriate heading command that steers the agents to the proper steady state behavior. By creating

a desired heading for the UAV, a reliable, robust heading controller can be used to track the heading commands. For a single UAV, a desired heading of the form

$$\psi^d = \psi^p + \tan^{-1}(kd) \tag{11}$$

will draw the agent onto the path, where d is the distance from the path and ψ^p is the heading along the path at $d = 0$ [8]. Using definition (8) equation (11) can be reduced to

$$\chi = \tan^{-1}(kd) \ . \tag{12}$$

Note that when d is large, the commanded heading is almost perpendicular to the heading along the path, effectively steering the UAV toward the path before beginning to follow it. For a simple orbit maneuver, ψ^p is selected to be tangent to the circle of interest along the ray connecting the agent and the target position. The radial distance of the agent from the nominal orbit constitutes d and a heading field constructed via (11) is shown in Figure 4. The gain k determines how aggressive the field is in steering the agent to the desired path.

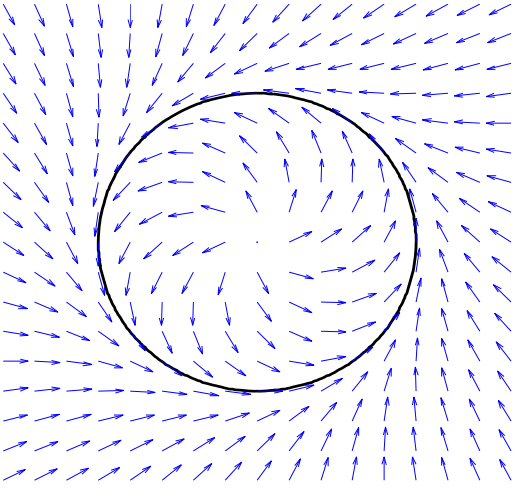

Fig. 4. A single UAV orbiting a stationary target has a commanded heading computed at each point given by (11). Note that when the agent is far from the orbit, the heading steers it toward the target. As it gets near the desired trajectory, the desired heading transitions to tangent to the nominal circular motion.

The constraint on ω is satisfied when

$$\max|\omega| = \max|\dot{\psi}^d| + \beta \leq \omega_{\max}$$

where $\omega_{\max} = \frac{g}{V_a}\tan(\phi_{\max})$ and β is the maximum control allowed for the feedback control term (see Equation (5)). Due to the relationship in Equation (11), the term $\max|\dot{\psi}^d|$ can be bounded by

$$\max|\dot{\psi}^d| < \max|\dot{\psi}^p| + \max|\dot{\chi}| \ .$$

The term $\max|\dot{\psi}^p|$ can be determined using *a priori* knowledge or an estimate of the path to be tracked (e.g. moving orbit, straight line, etc.); for stationary orbits, $|\dot{\psi}^p| = V_a/R_{\text{nom}}$. The term $\max|\dot{\chi}|$ directly depends on the strength of the field through the gain k. Recalling that $\chi = \tan^{-1}(kd)$ gives

$$|\dot{\chi}| = \left|\frac{k\dot{d}}{1+(kd)^2}\right| = \left|\frac{-kV_a \sin\chi}{1+(kd)^2}\right| \leq kV_a$$

which when coupled with knowledge of $\dot{\psi}^p$, the gain k can be chosen so as not to violate the UAV turn rate/roll angle constraints.

For a single UAV, a commanded heading of the form $\chi = \tan^{-1}(kd)$ guarantees asymptotic convergence to an orbit at radius R_{nom} about the target. A simple Lyapunov argument supports this assertion. Letting $W = \frac{1}{2}\chi^2$ and using (9) gives

$$\dot{W} = \chi\dot{\chi} = \frac{-kV_a\chi\sin\chi}{1+(kd)^2} \quad . \tag{13}$$

Since $\chi \in (-\pi/2, \pi/2)$ (χ is the output of an inverse tangent), the term $\chi\sin\chi$ is always greater than zero for nonzero χ. Therefore, $\dot{W} < 0$ and $\chi \to 0$ asymptotically. By LaSalle's invariance principle [9], it follows that $d \to 0$. Again we note that a complete proof for system (4) requires a sliding mode controller to guarantee that ψ reaches ψ^d in finite time, however, this can be relaxed as in [8]. Qualitatively, the commanded heading simply points the UAV directly toward the target if d is large and transitions to tangent to the orbit when near R_{nom}.

To account for spacing, the single agent heading command (11) is augmented as

$$\psi_i^d = \psi_i^p + \tan^{-1}(kd_i - \gamma\delta\theta_i) \tag{14}$$

where γ is a control gain weighting the value of spacing the UAVs to the value of converging to R_{nom}. The spacing term effectively increases the radius of the orbit when a UAV is too close to the agent in front of it and decreases the radius of the orbit if it is behind. This allows agents to "catch up" when the spacing is not at the desired state. An example of the heading field for an agent when $\delta\theta = \pi/2$ is shown in Figure 5. Notice the agent is drawn away from the nominal radius to allow the agent in front to increase its angular separation.

By constructing $\delta\theta_i$ to be only a function of its immediate neighbors, the error signal (heading field calculation) is local to each agent in the system. This allows the implementation to be completely decentralized. The advantage to decentralization is that the overall system will scale to any number of agents and be robust to insertion and deletion of team members. When agents are tasked to leave the formation for high priority assignments, the rest of the group can adjust to a new configuration without any centralized planning. Similarly, if a new agent is added (e.g. returns from a high priority task) the group will adjust through local interaction without any global communication.

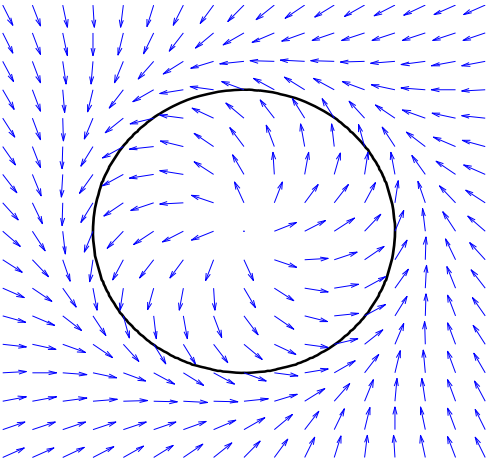

Fig. 5. A single UAV orbiting a stationary target with spacing error $\pi/2$ has desired heading given by (14). Note that a positive spacing error will cause the agent to effectively increase its radius, allowing the neighbor in front to gain distance and increase their relative spacing.

4 Stability Analysis

In the static target, no wind case, the splay state configuration coincides with the team members being equally spaced around an orbit. This section investigates the stability of the entire system when each agent follows the heading defined by (14). Figure 6 shows the behavior exhibited by a team of three UAVs.

A complete Lyapunov argument (or other method) may be used to determine the stability of the system to the splay state configuration. We have been unable to find a Lyapunov function that shows the stability of the entire system. For this reason, the convergence of the team of UAVs using (14) to the splay state configuration is argued as follows. We first show that the radial error is bounded by a function of the control gains k and γ. Near equilibrium, the overall system is shown to be exponentially stable. Finally, Monte-Carlo simulations are used to investigate system stability for initial conditions lying in the bounded region.

4.1 Ultimately Bounded

Lemma 1. *The system of agents described by (6) when following heading (14) is ultimately bounded in radial error d_i, i.e.*

$$|d_i| \leq R_\delta \tag{15}$$

where $R_\delta \triangleq \gamma\pi/k$ is less than R_{nom}.

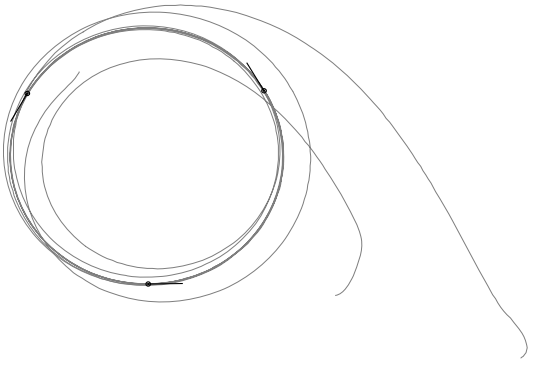

Fig. 6. Three UAVs following the heading defined by (14) converge to the splay state configuration along a non-moving orbit

Proof. For any agent, $\delta\theta_i$ is constrained to the region $(-\pi, \pi)$, i.e. agent cannot have an angular spacing error greater than π radians. If $|d_i| > R_\delta$, then

$$\begin{aligned} & \operatorname{sign}(k_i d_i - \gamma\delta\theta_i) = \operatorname{sign}(d_i) \\ \Rightarrow\ & \operatorname{sign}(\chi_i) = \operatorname{sign}(d_i) \\ \Rightarrow\ & \operatorname{sign}(\sin\chi_i) = \operatorname{sign}(d_i) \\ \Rightarrow\ & \operatorname{sign}(-V_a \sin\chi_i) = \operatorname{sign}(-d_i) \\ \Rightarrow\ & \operatorname{sign}(\dot{d}_i) = \operatorname{sign}(-d_i) \\ \Rightarrow\ & d_i \dot{d}_i < 0 \ . \end{aligned}$$

Therefore, the Lyapunov function $W = d_i^2$ has a negative definite derivative whenever d_i is outside the bound (15). When $|d_i| > \gamma\pi/k$, the kd_i terms dominates the $\gamma\delta\theta_i$ term in (14) effectively steering the UAV to reduce radial error regardless of spacing error. Therefore, $|d|$ is decreasing when $|d| > \gamma\pi/k$ and so all d_i are ultimately bounded to the region $(-R_\delta, R_\delta)$.

4.2 Local Stability

The splay state configuration in the no wind, non-moving target case corresponds to all the UAVs traveling on the orbit equally spaced, i.e. $d_i = 0$ and $\delta\theta_i = 0$ for all agents on the team. The change of variables introduced in Section 2.2 allows analysis of the system dynamics where each UAV has equations of motion determined by (9). Rewriting (9) using the definition of $\delta\theta_i$ in (10) to evaluate the error signals for each agent, we obtain

$$\begin{aligned} \dot{d}_i &= -V_a \sin\chi_i \\ \dot{\delta\theta}_i &= \frac{V_a}{R_i}\cos\chi_i - \tfrac{1}{2}\left[\frac{V_a}{R_{i+1}}\cos\chi_{i+1} + \frac{V_a}{R_{i-1}}\cos\chi_{i-1}\right] \ . \end{aligned} \tag{16}$$

In the calculation of the linearization of (16), it is helpful to compute the partial derivatives of χ_i with respect to the system state variables d_i and $\delta\theta_i$. Since

$\chi_i = \tan^{-1}(kd_i - \gamma\delta\theta_i)$, the partial derivatives evaluated at the equilibrium point $d_i = 0$, $\delta\theta_i = 0$ are calculated as

$$\begin{array}{rcl} \frac{\partial \chi_i}{\partial d_i} &=& k \\ \frac{\partial \chi_i}{\partial d_{\neg i}} &=& 0 \\ \frac{\partial \chi_i}{\partial \delta\theta_i} &=& -\gamma \\ \frac{\partial \chi_i}{\partial \delta\theta_{\neg i}} &=& 0 \end{array} \tag{17}$$

where $\neg i$ represents any value in $\mathcal{I}$ not equal to i. The partial derivative of $\dot{d}_i$ can be calculated as

$$\frac{\partial}{\partial *}\left(\dot{d}_i\right) = \frac{\partial}{\partial *}\left(-V_a \sin\chi_i\right) = -V_a \cos\chi_i \left(\frac{\partial}{\partial *}\chi_i\right) \ . \tag{18}$$

The matrix composing the partial derivatives of the system dynamics (16) has the structure

$$F = \begin{bmatrix} A & B \\ C & D \end{bmatrix} \triangleq \left[\begin{array}{c|c} \frac{\partial}{\partial d_i}(\dot{d}_i) & \frac{\partial}{\partial \delta\theta_i}(\dot{d}_i) \\ \hline \frac{\partial}{\partial d_i}(\dot{\delta\theta}_i) & \frac{\partial}{\partial \delta\theta_i}(\dot{\delta\theta}_i) \end{array}\right] \ . \tag{19}$$

Combining (18) with (17), the matrices A and B are calculated as $A = -kV_aI_N$ and $B = \gamma V_a I_N$ where I_N is the $N \times N$ identity matrix.

The linearization of the $\delta\theta$ dynamics reveals the ring structure inherent in the spacing calculation used to construct the desired heading. The function $\dot{\delta\theta}_i$ is composed of terms

$$\frac{V_a}{R_i}\cos\chi_i$$

which when linearized become

$$\frac{V_a}{R_i^2}\left(\frac{\partial}{\partial *}R_i\right)\cos\chi_i - \frac{V_a}{R_i}\sin\chi_i\left(\frac{\partial}{\partial *}\chi_i\right) \ .$$

At the equilibrium, the only term that does not become zero is the term containing $\partial R_i/\partial d_i$. Note that since R_i does not depend on $\delta\theta_i$, the partial derivative with respect to $\delta\theta_i$ will be zero. The linearized dynamics of $\delta\theta_i$ become

$$\begin{array}{rcl} \frac{\partial}{\partial d_i}\left(\dot{\delta\theta}_i\right) &=& \frac{-V_a}{{R_{\text{nom}}}^2} \\ \frac{\partial}{\partial d_{i\pm1}}\left(\dot{\delta\theta}_i\right) &=& \frac{1}{2}\frac{V_a}{{R_{\text{nom}}}^2} \\ \frac{\partial}{\partial \delta\theta_i}\left(\dot{\delta\theta}_{i,\neg i}\right) &=& 0 \ . \end{array} \tag{20}$$

We conclude that the matrix D in (19) is simply the zero matrix of size $N \times N$ and matrix C is a circulant matrix

$$C = \frac{1}{2}\frac{V_a}{{R_{\text{nom}}}^2}\begin{bmatrix} -2 & 1 & 0 \cdots 0 & 1 \\ 1 & -2 & 1 \cdots 0 & 0 \\ \vdots & \vdots & \vdots \ddots \vdots & \vdots \\ 1 & 0 & 0 \cdots 1 & -2 \end{bmatrix} \ . \tag{21}$$

Of particular note is the structure of C

$$C = \frac{1}{2}\frac{V_a}{{R_{\text{nom}}}^2}\left(-2I_N + \mathcal{C}_N\right) \tag{22}$$

where

$$\mathcal{C}_N = \begin{bmatrix} 0\,1\,0\cdots 0\,1 \\ 1\,0\,1\cdots 0\,0 \\ \vdots\;\vdots\;\vdots\;\ddots\;\vdots\;\vdots \\ 1\,0\,0\cdots 1\,0 \end{bmatrix} \tag{23}$$

is the adjacency matrix corresponding to the ring graph of size N. The eigenvalues of F can be formulated in terms of the eigenvalues of C which are known using results from algebraic graph theory [10].

Lemma 2. *Consider the matrix*

$$F = \begin{bmatrix} -kV_aI_N & \gamma V_aI_N \\ C & 0_N \end{bmatrix} \tag{24}$$

where C is given by (21), I_N is the $N \times N$ identity matrix and 0_N is an $N \times N$ matrix of zeros. The eigenvalues of F are given by

$$\lambda_j = -\frac{1}{2}kV_a \pm \sqrt{\left(\frac{1}{2}kV_a\right)^2 + \gamma V_a\mu_j} \quad \text{for } j = 1\ldots N \tag{25}$$

where

$$\mu_j = \frac{1}{2}\frac{V_a}{{R_{\text{nom}}}^2}\left(2\cos\left(\frac{2\pi}{N}(j-1)\right) - 2\right) \tag{26}$$

is an eigenvalue of C.

Proof. We begin by showing that the eigenvalues of C are given by (26). From (22) we conclude that

$$\mu_j = \frac{1}{2}\frac{V_a}{{R_{\text{nom}}}^2}\left(-2 + \gamma_j\right)$$

where γ_j is an eigenvalue of $\mathcal{C}_N$. Results from algebraic graph theory show that the eigenvalues of $\mathcal{C}_N$ are

$$\gamma_j = 2\cos\left(\frac{2\pi}{N}(j-1)\right) \quad \text{for } j = 1\ldots N \ .$$

Let λ be an eigenvalue of F and x its corresponding eigenvector. Partition x into blocks corresponding with the blocks of F, i.e. $x = \begin{bmatrix} x_d^T & x_{\delta\theta}^T \end{bmatrix}^T$ where both x_d and $x_{\delta\theta}$ are of length N. The eigenvector relationship $Fx = \lambda x$ can be written

$$-kV_ax_d + \gamma V_ax_{\delta\theta} = \lambda x_d \ \Rightarrow\ \gamma V_ax_{\delta\theta} = \left(\lambda + kV_a\right)x_d \tag{27}$$

$$Cx_d = \lambda x_{\delta\theta} \ . \tag{28}$$

From (27) we see that

$$x_{\delta\theta} = \frac{\lambda + kV_a}{\gamma V_a} x_d \tag{29}$$

which when applied to (28) yeilds

$$Cx_d = \left(\frac{\lambda(\lambda + kV_a)}{\gamma V_a} \right) x_d \ .$$

Note that this is exactly the eigenvector relationship for the matrix C where $Cx = \mu x$ for

$$\mu = \left(\frac{\lambda(\lambda + kV_a)}{\gamma V_a} \right) \ .$$

Solving this for λ yields Equation (25).

Theorem 1. *Consider the matrix F as defined in (24). All eigenvalues except for $\lambda = 0$ of F are located in the open left half plane. Additionally, the eigenvectors associated with $\lambda = 0$ and $\lambda = -kV_a$ span a subspace of $\mathbb{R}^{2N}$ orthogonal to the remaining $2N - 2$ eigenvectors of F.*

Proof. Equation (25) gives the relationship of the eigenvalues of F to the eigenvalues of C. Only a single eigenvalue of C is equal to zero, all other $N - 1$ values are strictly less than zero. The zero eigenvalue in C maps to the eigenvalues $\lambda = -kV_a$ and $\lambda = 0$ in F. The remaining eigenvalues of C (all strictly less than zero) have discriminant strictly less than $(\frac{1}{2}kV_a)^2$ thus ensuring that each λ has real part in the open left half plane.

The proof of Lemma 2 gives the relationship between the eigenvectors of C and those of F via (29) where x_d is the eigenvector of C corresponding to eigenvalue

$$\mu = \left(\frac{\lambda(\lambda + kV_a)}{\gamma V_a} \right) \ .$$

Since C is a symmetric matrix, its eigenvectors form an orthonormal basis of $\mathbb{R}^N$. Note that C has constant row sums of zero, so the eigenvector associated with the zero eigenvalue of C is the vector of all ones, $\mathbf{1}$. Due to the orthogonality of the eigenvectors of C, $\mathbf{1}^T u_j = 0$ for all eigenvectors of C, $u_j \neq \mathbf{1}$. Using (29), the eigenvectors for $\lambda = 0$ and $\lambda = -kV_a$ are

$$x_0 = \begin{bmatrix} \mathbf{1} \\ \frac{k}{\gamma}\mathbf{1} \end{bmatrix}, \quad x_{-kV_a} = \begin{bmatrix} \mathbf{1} \\ \mathbf{0} \end{bmatrix} \ . \tag{30}$$

The inner product of these eigenvectors with all other eigenvectors of F can be written as

$$\begin{bmatrix} \mathbf{1}^T & \frac{k}{\gamma}\mathbf{1}^T \end{bmatrix} \begin{bmatrix} u_j \\ \frac{\lambda + kV_a}{\gamma V_a} u_j \end{bmatrix} = 0 \quad \text{and} \quad \begin{bmatrix} \mathbf{1}^T & \mathbf{0}^T \end{bmatrix} \begin{bmatrix} u_j \\ \frac{\lambda + kV_a}{\gamma V_a} u_j \end{bmatrix} = 0 \ .$$

Corollary 1. *The linearization of system (16) is exponentially stable.*

Proof. Linearization of (16) yields the state equation $\dot{x} = Fx$ where F is given in equation (24), and whose solution is $x(t) = e^{Ft}x_0$. By Theorem 1 all but one eigenvalue is in the open left half plane, so any part of the initial condition x_0 that lies in the span of the eigenvectors associated with those eigenvalues exponentially decays to zero. By definition of $\delta\theta_i$, the constraint

$$\sum_{i=1}^{N} \delta\theta_i = 0 \tag{31}$$

must hold for any state vector associated with the original system. The eigenvectors associated with $\lambda = 0$ and $\lambda = -kV_a$ are given in (30). These eigenvectors form a subspace orthogonal to all other eigenvectors in the linearized system. To lie in the subspace spanned by the eigenvectors (30), all $\delta\theta_i$ must be equal. However, the only vector $\boldsymbol{\delta\theta}$ that satisfies the constraint (31) and is in this subspace is $\boldsymbol{\delta\theta} = \mathbf{0}$, which is either along the eigenvector associated with $\lambda = -kV_a$ or in the subspace spanned by the remaining eigenvectors of the system. In other words, it is impossible to have an initial condition in the subspace spanned by the eigenvector associated with $\lambda = 0$. Therefore, the initial condition x_0 lies in the space spanned by eigenvectors whose eigenvalues are in the open left half plane and the linearized system is exponentially stable.

4.3 Global Stability

The system (16) is ultimately bounded to $d_i \in (-R_\delta,\ R_\delta)$, $\delta\theta_i \in (-\pi,\ \pi)$ and locally asymptotically stable. Monte-Carlo simulations are used to infer the stability of the system in the remaining region between the ultimate bound and the equilibrium path.

The Monte-Carlo simulations use the model (4) with desired heading given by (14). For team sizes $N = 2$, 3, 4, 5, and 6, a set of 10,000 simulations with random initial conditions in d_i and $\delta\theta_i$ were run to verify the stability of the system. An error metric

$$e(t) = \sqrt{\sum_{i=1}^{N} d_i(t)^2 + \delta\theta_i(t)^2}$$

captures the error from the splay state configuration at time t. The largest error at $t = 100$ seconds over all 50,000 simulations was $2e^{-4}$ indicating that the actual region of convergence is likely to be global.

5 Extension to Moving Targets

The ability for a UAV to orbit a target in the presence of wind or target motion is crucial. Modifications to the static target, no wind case can be made to allow UAVs to track moving targets.

To extend the approach of (14) to moving targets, the path heading term ψ^p must be calculated to allow a UAV to remain on a moving orbit. Essentially, the steady state behavior of a UAV on the orbit is determined by ψ^p: while following ψ^p at $d = 0$, a UAV should remain on the moving orbit.

Consider the behavior of a particle orbiting a constant speed target at fixed radius R_n then

$$\begin{aligned} x^p(t) &= R_n \cos(\theta(t)) + W_x t \\ y^p(t) &= R_n \sin(\theta(t)) + W_y t \end{aligned} \tag{32}$$

where W_x and W_y are the velocity of the orbit center. Differentiating (32) results in the expression

$$\begin{aligned} \dot{x}^p &= -R_n \dot{\theta} \sin\theta + W_x \\ \dot{y}^p &= R_n \dot{\theta} \cos\theta + W_y \ . \end{aligned} \tag{33}$$

The path heading is chosen as

$$\psi^p = \tan^{-1}\left(\frac{\dot{y}^p}{\dot{x}^p}\right) \tag{34}$$

which is the direction of the vector that is tangent to the moving orbit. To ensure that the UAV maintains constant airspeed, the magnitude of the tangent vector must equal V. This constraint allows the calculation of $\dot{\theta}$ from (33) as

$$\begin{aligned} & V_a^2 = (\dot{x}^p)^2 + (\dot{y}^p)^2 = \left(-R_n\dot{\theta}\sin\theta + W_x\right)^2 + \left(R_n\dot{\theta}\cos\theta + W_y\right)^2 \\ & \Rightarrow \dot{\theta}^2\left(R_n^2\right) + \dot{\theta}\left(2R_nW_y\cos\theta - 2R_nW_x\sin\theta\right) + \left(W_x^2 + W_y^2 - V_a^2\right) = 0 \\ & \Rightarrow \dot{\theta} = -\tfrac{1}{R_n}\left(W_y\cos\theta - W_x\sin\theta\right) \pm \\ & \qquad \tfrac{1}{R_n}\sqrt{\left(W_y\cos\theta - W_x\sin\theta\right)^2 - \left(W_x^2 + W_y^2 - V_a^2\right)} \ . \end{aligned} \tag{35}$$

The discriminant in (35) shows that when the magnitude of the velocity of the target is greater than the speed of the UAV, a real solution does not exist. In practical terms, this means that for the agent to properly maintain its orbit around the target, the speed of the wind plus the speed of the target cannot exceed the speed of the UAV.

The turn rate constraint of the UAV must also be accounted for in determining the allowable magnitude of motion that can be feasibly tracked. Disregarding the other components of heading rate,

$$\left|\dot{\psi}^p\right| \leq \frac{g}{V_a}\tan(\phi_{\max}) \tag{36}$$

ensures that the path satisfies the turn rate constraints. The maximum value of $\dot{\psi}^p$ depends on V_w, the magnitude of the motion in the system (note $V_w^2 = W_x^2 + W_y^2$). To ensure that the orbit can feasibly be followed with regard to the turn constraints of the UAV, V_w must satisfy

$$\frac{(2V_w + V_a)(V_w + V_a)^2}{R_n V_a^2} \leq \frac{g}{V_a}\tan(\phi_{\max}) \ . \tag{37}$$

Intuitively, a UAV can follow a moving target in wind if the magnitude of the wind and target velocity are not too great to violate the velocity or turn rate constraints of the UAV. For example, a UAV with maximum bank angle of 35 degrees, airspeed of 15 meters per second and desired orbit of 100 meters can track a target with speed less than 5.17 m/s.

With ψ^p determined by (34), a desired heading of (11) can be used for a single UAV to follow a moving target in the presence of wind given that the turn rate constraint of the UAV is satisfied. For multiple UAVs, the definition of the splay state configuration is used to develop a spacing error term. Note that achieving equal angle spacing around a moving orbit is impossible when the velocity of the UAVs is held constant. For this reason, the actual time along the steady-state orbit between neighbors is used to compute the error from the splay state configuration. Similar to the static target case, the timing error is computed by assuming that all UAVs are on the desired orbit (i.e. $d_i = 0$). Consider two agents on the orbit with clock angles θ_i and θ_j. The time difference from agent i to agent j is given by $T_{i\to j} = t - t_0$ such that $\theta(t) = \theta_j$ where $\theta(t)$ is determined by solving the initial value problem

$$\begin{aligned} \dot{\theta} = &-\tfrac{1}{R_n}\left(W_y \cos\theta - W_x \sin\theta\right) \pm \\ &\tfrac{1}{R_n}\sqrt{\left(W_y \cos\theta - W_x \sin\theta\right)^2 - \left(W_x^2 + W_y^2 - V_a^2\right)} \\ \theta(t_0) = \theta_i \ . & \end{aligned} \tag{38}$$

The timing error for a specific agent i can then be defined as

$$\delta t_i = \frac{1}{2}\left(T_{(i-1)\to i} - T_{i\to(i+1)}\right) \ . \tag{39}$$

The δt term is used in exactly the same manner as the $\delta\theta$ term in the static target case, i.e. a desired heading is calculated as

$$\psi_i^d = \psi_i^p + \tan^{-1}(kd_i - \gamma\delta t_i) \ . \tag{40}$$

Many of the stability notions from the non-moving target case carry over to the moving target case. A maximum δt exists since agents can only be of finite angle apart. Therefore, for large errors in radial distance d, the kd_i term will dominate the heading calculation and force the system to be ultimately bounded. A linearization of the system dynamics for the moving target case also shows many similarities to static case. In particular the upper two blocks of the state matrix are identical to the blocks in the static target linearization. We postulate that the lower blocks are identical up to a positive scale factor, i.e. the circulant structure of the lower left block is preserved which allows us to conclude linear stability via the same arguments as in the static target case. Additionally, Monte-Carlo simulations are used to indicate that the system converges to the splay state configuration in the moving target case. For team sizes $N = 2$, 3, and 4, a set of 1,000 simulations with random initial conditions in d_i, δt_i and V_w were run to verify the stability of the system. An error metric

$$e(t) = \sqrt{\sum_{i=1}^{N} \delta t_i(t)^2}$$

captures the error from the splay state configuration at time t. The largest error at $t = 100$ seconds over 3,000 simulations was 0.5 indicating that control (40) leads to convergence to the splay state configuration. Figure 7 shows typical behavior of 4 UAVs orbiting a moving target. The timing error from the splay state configuration for this scenario is shown in Figure 8.

Fig. 7. Trajectories of 4 UAVs orbiting a moving target trace out routes similar to those in this figure

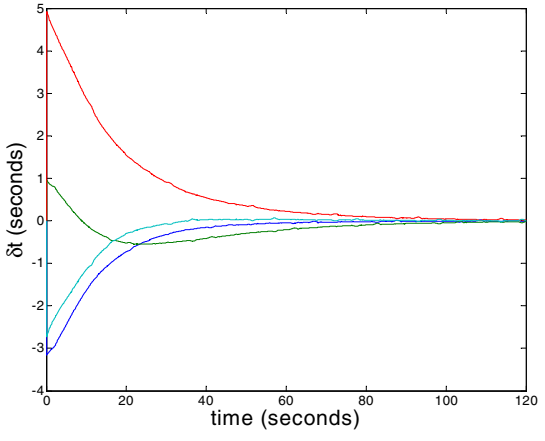

Fig. 8. Error from the splay state configuration for 4 UAVs tracking a moving target is driven to zero using (40)

6 Simulation Results

The splay state controller is based upon choosing a heading that draws the UAVs to the splay state configuration. The design of the heading command is accomplished by assuming a simple kinematic model given by (4). To validate the design, the splay state controller is tested in high fidelity simulation. Each UAV is simulated with full 6 degree of freedom dynamics model with aerodynamic parameters that match the small UAVs flown at BYU [11]. Additionally, the human interface and autopilot code are emulated to match actual flight conditions as closely as possible.

Trajectories of 3 UAVs that loiter at fixed locations and are then commanded to reach the splay state configuration are shown in Figure 9. The radial error of

a UAV is approximately one meter and the spacing error about 3 degrees. These errors are due mainly to the update rate of the team - each UAV only communicates to its neighbors when a new GPS packet is received at approximately 1 Hertz.

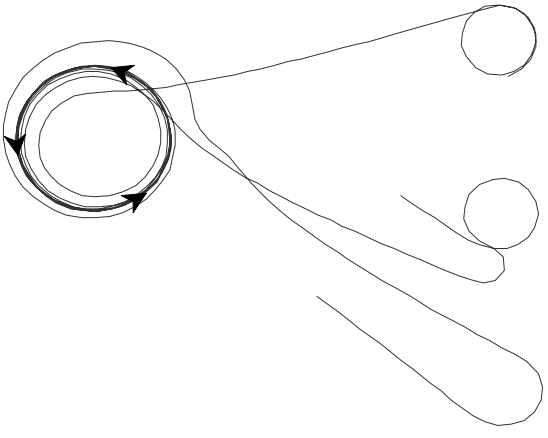

Fig. 9. High fidelity simulation results of the splay state controller indicate that the method can be effective in actual implementation

Despite design of the splay state controller in a low-order environment, application of the control in high fidelity simulation shows that the splay state controller may be effective in hardware implementation.

7 Conclusions and Future Work

This chapter has developed a decentralized splay state controller for a team of UAVs monitoring a target. In the static case (i.e. non-moving target and no wind), the controller spaces UAVs equally around an orbit centered on the target. The decentralized nature of the control strategy allows the the team to be robust to insertion, deletion and re-assignment of team members. The controller is shown to be linearly stable in the static target case and Monte-Carlo simulations indicate global stability in all cases. By defining an appropriate measure of spacing around the orbit, the splay state configuration can be reached for moving targets in the presence of wind. High fidelity simulation results show that the controller may be practical in actual hardware implementation.

There are still many open questions in regards to the convergence of a team of UAVs to the splay state configuration. Monte-Carlo simulations indicate that the region between the ultimate bound and the equilibrium is stable, but a formal proof of this assertion remains an open problem. Additionally, the design of the commanded heading is based on a low-order UAV model. Extending the analysis to the model (1) and finding an appropriate control u, rather than relying on a sliding mode inner-loop control, is also an important extension.

Acknowledgements

This work is partially funded by the National Science Foundation under Information Technology Research Grant CCR-0313056 and by the Air Force Office of Scientific Research award No. FA9550-04-0209.

References

1. Frew, E.W., Lawrence, D.A.: Cooperative stand-off tracking of moving targets by a team of autonomous aircraft. In: Proceedings of the AIAA Guidance, Navigation, and Control Conference. (2005)
2. Tang, Z., Ozguner, U.: Motion planning for multitarget surveillance with mobile sensor agents. IEEE Transactions on Robotics (October 2005)
3. Gu, G., Chandler, P.R., Schumacher, C., Sparks, A., Pachter, M.: Optimal cooperative sensing using a team of UAVs. IEEE Transactions on Aerospace and Electronic Systems (October 2006)
4. Sepulchre, R., Paley, D.A., Leonard, N.E.: Stabilization of planar collective motion: All-to-all communication. IEEE Transactions on Automatic Control (June 2007)
5. Klein, D.J., Morgansen, K.A.: Controlled collective motion for trajectory tracking. In: Proceedings of the IEEE American Control Conference. (2006)
6. Yang, G., Kapila, V.: Optimal path planning for unmanned air vehicles with kinematic and tactical constraints. In: Proceedings of the IEEE Conference on Decision and Control. (2002)
7. Chandler, P.R., Pachter, M., Rasmussen, S.: UAV cooperative control. In: Proceedings of the IEEE American Control Conference. (2001)
8. Griffiths, S.R.: Vector field approach for curved path following for miniature aerial vehicles. In: Proceedings of the AIAA Guidance, Navigation, and Control Conference. (2006)
9. Khalil, H.K.: Nonlinear Systems. Prentice Hall (1996) Theorem 4.4, p. 128.
10. Godsil, C., Royle, G.: Algebraic Graph Theory. Springer-Verlag New York, Inc. (2001)
11. Beard, R., Kingston, D., Quigley, M., Snyder, D., Christiansen, R., Johnson, W., Mclain, T., Goodrich, M.: Autonomous vehicle technologies for small fixed wing UAVs. AIAA Journal of Aerospace Computing, Information, and Communication (2005)